Atmos. Chem. Phys., 14, 13223–13240, 2014
www.atmos-chem-phys.net/14/13223/2014/
doi:10.5194/acp-14-13223-2014

Atmospheric Chemistry and Physics
Open Access

Tropical deep convective life cycle: Cb-anvil cloud microphysics from high-altitude aircraft observations

W. Frey[1,2], S. Borrmann[1,3], F. Fierli[4], R. Weigel[3], V. Mitev[5], R. Matthey[6], F. Ravegnani[7], N. M. Sitnikov[8], A. Ulanovsky[8], and F. Cairo[4]

[1]Max Planck Institute for Chemistry, Mainz, Germany
[2]School of Earth Sciences and ARC Centre of Excellence for Climate System Science, University of Melbourne, Melbourne, Australia
[3]Institute for Atmospheric Physics, Johannes Gutenberg University, Mainz, Germany
[4]Institute of Atmospheric Sciences and Climate, ISAC-CNR, Rome, Italy
[5]Swiss Centre for Electronics and Microtechnology, Neuchâtel, Switzerland
[6]Laboratoire Temps-Fréquence, Institute de Physique, Université de Neuchâtel, Neuchâtel, Switzerland
[7]Institute of Atmospheric Sciences and Climate, ISAC-CNR, Bologna, Italy
[8]Central Aerological Observatory, Dolgoprudny, Moscow Region, Russia

Correspondence to: W. Frey (wiebke.frey@unimelb.edu.au)

Received: 24 April 2014 – Published in Atmos. Chem. Phys. Discuss.: 12 May 2014
Revised: 3 November 2014 – Accepted: 5 November 2014 – Published: 11 December 2014

Abstract. The case study presented here focuses on the life cycle of clouds in the anvil region of a tropical deep convective system. During the SCOUT-O3 campaign from Darwin, Northern Australia, the Hector storm system has been probed by the Geophysica high-altitude aircraft. Clouds were observed by in situ particle probes, a backscatter sonde, and a miniature lidar. Additionally, aerosol number concentrations have been measured. On 30 November 2005 a double flight took place and Hector was probed throughout its life cycle in its developing, mature, and dissipating stage. The two flights were four hours apart and focused on the anvil region of Hector in altitudes between 10.5 and 18.8 km (i.e. above 350 K potential temperature). Trajectory calculations, satellite imagery, and ozone measurements have been used to ensure that the same cloud air masses have been probed in both flights.

The size distributions derived from the measurements show a change not only with increasing altitude but also with the evolution of Hector. Clearly different cloud to aerosol particle ratios as well as varying ice crystal morphology have been found for the different development stages of Hector, indicating different freezing mechanisms. The development phase exhibits the smallest ice particles (up to 300 µm) with a rather uniform morphology. This is indicative for rapid glaciation during Hector's development. Sizes of ice crystals are largest in the mature stage (larger than 1.6 mm) and even exceed those of some continental tropical deep convective clouds, also in their number concentrations. The backscatter properties and particle images show a change in ice crystal shape from the developing phase to rimed and aggregated particles in the mature and dissipating stages; the specific shape of particles in the developing phase cannot be distinguished from the measurements. Although optically thin, the clouds in the dissipating stage have a large vertical extent (roughly 6 km) and persist for at least 6 h. Thus, the anvils of these high-reaching deep convective clouds have a high potential for affecting the tropical tropopause layer by modifying the humidity and radiative budget, as well as for providing favourable conditions for subvisible cirrus formation. The involved processes may also influence the amount of water vapour that ultimately reaches the stratosphere in the tropics.

1 Introduction

Deep convection provides a fast pathway to transport air masses from the boundary layer through the free troposphere into the tropopause region, sometimes with overshooting

into the stratosphere (Corti et al., 2008; Fueglistaler et al., 2009). Thus, trace gases, water vapour, and aerosols are redistributed effectively in the atmosphere. Clouds form in this convective environment and may build large cloud shields, which have an important impact on the radiation balance, regulating incoming solar and outgoing long-wave radiation (Baker, 1997; Baker and Peter, 2008), and on the regional chemistry (including ozone; e.g. Solomon et al., 1997), also in the tropics (von Hobe et al., 2011). Furthermore, water and condensable gases as well as aerosols are removed from the gas phase by adsorption onto or scavenging by the cloud particles. In what manner ice clouds impact climate and chemistry critically depends on the clouds' microphysics, i.e. sizes and numbers, as well as shapes of the ice particles. Cloud microphysics also determines the amount of water vapour that passes through the Tropical Tropopause Layer (TTL) into the stratosphere (Corti et al., 2008; Jensen et al., 2008; de Reus et al., 2009; Davis et al., 2010). Hence it is essential to have detailed information on the cloud microphysical properties, for example to realistically represent the tropical high-altitude clouds in numerical models (e.g. van Diedenhoven et al., 2012). In this respect the results of in situ measurements are of particular importance despite the availability of cloud observations from satellite or ground-based instruments, which are unable to resolve the microphysical structures.

The TTL is usually defined at altitudes between 14 and 18 km and it is the dominant source region of air entering the stratosphere (Park et al., 2007; Fueglistaler et al., 2009). The level of zero radiative heating and the cold point tropopause are located within the TTL. Typical residence times for air parcels in the TTL are roughly 2 months (Krüger et al., 2009). Furthermore, the lowest TTL altitude levels have been identified as a region where frequent new particle formation events occur in clear air as well as in cumulonimbus (Cb) cloud anvils (Weigel et al., 2011; Frey et al., 2011), with unknown consequences for the aerosol in the lower stratosphere. Previous observational studies involving aircraft often focussed only on the development and mature stages of tropical convection, or even just on parts of the convective clouds, e.g. convective overshooting, but little attention has been paid to the dissipating stage. So the question remains what the microphysical properties of convective clouds in the tropical tropopause layer look like, especially throughout their lifetime.

Additionally, the ice formation processes within deep convective clouds are not completely understood (van Diedenhoven et al., 2012), for example regarding glaciation temperatures. While some studies suggest rapid glaciation in the updrafts when the air reaches the freezing level (e.g. Stith et al., 2004), others show the possibility of supercooled liquid water to reach the homogeneous drop freezing temperature (about $-38\,^{\circ}\mathrm{C}$) in the case of strong updrafts (Heymsfield et al., 2009). This is possibly due to shorter transit times in the stronger updrafts that allow the liquid drops to reach higher altitudes. When pre-existing ice is present at temperatures $> -38\,^{\circ}\mathrm{C}$ (e.g. by entrainment from downdrafts or uplift of heterogeneously frozen ice from lower levels), homogeneous freezing can be suppressed. However, in strong updrafts the pre-existing ice might be unable to cause depletion of water vapour and suppressed droplet activation (Heymsfield et al., 2005). The role of homogeneous droplet freezing may change throughout the cloud life time (e.g. being more important in young updrafts), and is also dependent on the air flow around the convection (Heymsfield et al., 2005). At lower temperatures ($T \ll -38\,^{\circ}\mathrm{C}$) in situ formation of ice particles can occur by freezing of solution droplets (Koop et al., 2000). As air is pushed upwards, sufficiently low temperatures and high relative humidities can be reached. Once the deep convective cloud ages and the anvil loses a large fraction of its ice water content (IWC) by sedimentation, new ice nucleation can occur, as observed by Gallagher et al. (2012) in the cloud edge region. Thus, eventually not enough ice particles are left to reduce water vapour excess and suppress homogeneous freezing, as in the high updraft scenario mentioned above. Therefore, it can be expected that such a complex history of freezing processes in a convective cloud system leads to highly variable cloud particle shapes and size distributions throughout the life cycle of an anvil.

As with the observational studies, the focus of numerical experiments rarely touches the dissipating stage and thus does not cover the complete life cycle of the convective clouds. For example, when looking at simulations of Hector thunderstorms, a deep convective system (Keenan et al., 1994; Carbone et al., 2000) that can be found over the Tiwi Islands, Northern Australia. Saito et al. (2001) point out the sensitivity of the storm development to ice phase physics and island-scale circulations; however, when coming to the dissipating stage they state: "Since the decay of convection is not the primary interest, it is not examined further." Other reasons for not looking into the dissipating state may involve models failing to predict the dissipating stage correctly (e.g. Chemel et al., 2009). Connolly et al. (2013) suggest that microphysics schemes may produce anvils that have an extent and persistence which is too small due to the assumed density of snow. However, the dissipation of a deep convective system may have major implications for the formation of subvisible cirrus (SVC), by affecting the background conditions, for example regarding humidity and the availability of processed aerosols (after cloud dissipation). These cirrus are found close to the tropical cold point tropopause and can occur in widespread layers, though vertically only reaching a depth of a few hundred metres (Winker and Trepte, 1998; Thomas et al., 2002). Their importance for radiative effects and dehydration of tropopause air which is further transported into the stratosphere is a point of discussion (Rosenfield et al., 1998; Corti et al., 2006; Davis et al., 2010). SVC can be formed either in situ or due to blow-off from deep convection, the partitioning of the two depending on the region. For instance, Massie et al. (2002) found that half of the

SVC observations by the Halogen Occultation Experiment (HALOE) over the maritime continent are consistent with formation via convective blow-off. Over the east Pacific, a generally less convectively active region, Global Hawk observations indicate that most likely SVC have formed in situ (Jensen et al., 2013). By contrast, similar aircraft observations in the Seychelles region over the Indian Ocean demonstrated the occurrence of SVC in the vicinity of mesoscale convective systems (MCS) (Thomas et al., 2002). Jensen et al. (1996) simulated the formation of SVC from remnants of deep convective clouds. They point out the role of wind shear in formation of cloud layers with vertical thicknesses less than 1 km by convective blow-off. Thus, gaining more insight into the dissipating stage of deep convective systems will also be helpful for understanding SVC formation. Aged convective anvils may transform into SVC, or changed background conditions regarding humidity and processed aerosols after dissipation of the anvils may facilitate in situ formation of SVC.

After the dissipation of large cloud systems, like Hector, patches of "left over clouds" and of enhanced numbers of larger, swollen, humidified aerosol particles may remain in the air mass of the original deep convective cloud. The radiative effects of this air, which is not yet completely cloud free, will be different from clear air and from cloudy air resembling more the "twilight zone" brought forward by Koren et al. (2007). Satellite observations may find cloud-free pixels next to cloudy pixels that are actually the twilight zone, i.e. containing undetectable clouds and aerosol. These areas show elevated reflectance and have been found to be unreliable for aerosol retrievals (Koren et al., 2007; Wen et al., 2006). For these reasons closer consideration of the dissipation stages of cloud systems is important from the perspective of the radiative budget and also of the satellite data retrieval and analyses.

This work is a case study using in situ observations of a Hector thunderstorm obtained during two consecutive flights on 30 November 2005 from the anvil region (between 350 and 375 K potential temperature). The purpose is to (1) document and provide data about the microphysical properties of a deep convective cloud in the TTL throughout its life cycle (e.g. for numerical simulations), (2) study the potential for SVC formation, and (3) investigate the freezing mechanisms inside the MCS.

2 Experiment and instrumentation

2.1 SCOUT-O3 campaign

As part of the European integrated project Stratospheric–Climate Links with Emphasis on the Upper Troposphere and Lower Stratosphere (SCOUT-O3; Brunner et al., 2009) an aircraft campaign was conducted from Darwin, Northern Australia in November/December 2005. The main objectives of this campaign were to investigate the transport and transformation of trace gases, water vapour, and aerosols through the TTL and the role of deep convection therein. Darwin was chosen as the base for the experiment due to its proximity to the Tiwi Islands and the Hector storm system which develops on an almost daily basis during premonsoon season above those islands. Hector develops mostly as a consequence of an interaction between sea breeze fronts and convectively generated cold pools above the islands (Carbone et al., 2000). The aircraft probing the air masses over and in the vicinity of the Tiwi Islands and the Hector system was the Russian M55 "Geophysica" high-altitude research aircraft with a ceiling of 20 km. The Geophysica performed nine flights with different foci, i.e. studying convection and long-range transport and performing satellite validation. Brunner et al. (2009) describe the large-scale meteorological context of the campaign; details of the meteorological context for this study can be found in Sect. 3.

2.2 Instrumentation

2.2.1 Cloud particle instrumentation

Two instruments were used to observe cloud particles: a modified Particle Measuring Systems (PMS) Forward Scattering Spectrometer Probe (FSSP-100) with Droplet Measurement Technologies (DMT) high-speed electronics (SPP-100), and a DMT Cloud Imaging Probe (CIP). The instruments cover a size range (in diameter D_p) of $2.7\,\mu m < D_p < 29.2\,\mu m$ (FSSP-100) and $25\,\mu m < D_p < 1600\,\mu m$ with a 25 µm resolution (CIP). The characteristics of both instruments are described in de Reus et al. (2009) and Frey et al. (2011, and references therein). Since the FSSP-100 sampled data in a 2 s interval, the CIP data have been averaged over 2 s as well in order to combine with the FSSP-100 measurements. Particle diameters are derived from the CIP images using the maximum dimension (Heymsfield et al., 2002). Sizing of FSSP particles has been performed assuming the particles to be spherical. Considering the scattering cross-sections from T-matrix and Mie curves with a refractive index of ice, the original 40 size bins have been redefined into seven size bins, to account for ambiguities. An ice density of $0.917\,g\,cm^{-3}$ was used to calculate the ice water content (IWC), assuming sphericity in the FSSP size range and using an image to mass relationship as introduced by Baker and Lawson (2006) for the larger particles. The uncertainties of the measured number concentrations are mainly determined by the uncertainties in the sample volumes, which were estimated to be 20 % (Baumgardner et al., 1992; de Reus et al., 2009) for both probes. Additional uncertainty due to counting statistics has been taken into account, especially in conditions with low particle number concentrations. For the calculation of size distributions integration times have been adequately extended, depending on the particular conditions of each measurement period dur-

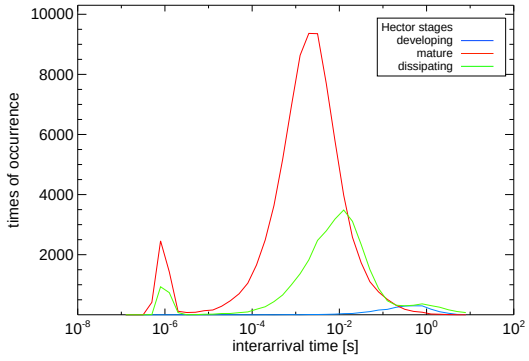

Figure 1. Frequency distributions of interarrival times used to identify shattering artefacts in the CIP image data. The data are grouped into Hector classification stages as described in Sect. 4.1.

ing the flight. The cloud particle data have been thoroughly filtered for shattering artefacts, following the interarrival time approach (Field et al., 2006), since the probe came with the original tips (i.e. not anti-shattering optimised). Frequency distributions of interarrival times for the different Hector development stages (as outlined in Sect. 4.1) are shown in Fig. 1. Shattered particles can be clearly identified by the secondary peak around 10^{-6} s. Furthermore, as shown by de Reus et al. (2009) and Cairo et al. (2011), who used comparisons of the cloud particle data from CIP and FSSP to lyman-alpha hygrometers and a backscatter sonde respectively, shattering was not a problem for these particular samplings of Hector clouds. A further set of corrections has been applied to the CIP images, i.e. accounting for the loss of the first slice (due to slow acquisition start-up time), empty images (reconstructed as one pixel image), partial images, out of focus images, airspeed, and too small an area ratio (rejection of streakers). A detailed description of these corrections and the capability of the instruments to measure reliably under the conditions in the upper troposphere and lower stratosphere can be found in Frey et al. (2011, and the accompanying supplement material, which also includes an extensive discussion of possible shattering artefacts).

2.2.2 Backscatter sonde

Further cloud properties were measured by the Multiwavelength Aerosol Scatterometer (MAS; Cairo et al., 2004; Buontempo et al., 2006). This backscatter sonde obtains in situ measurements of optical properties and microphysical parameters of aerosol and cloud particle ensembles, e.g. backscatter ratio and depolarisation (at 532 and 1064 nm). MAS samples with a time resolution of 5 s and has a precision of 10 %.

2.2.3 Miniature lidar

The downward looking Miniature Aerosol Lidar (MAL; Mitev et al., 2002) detects vertical profiles of aerosol and cloud particles below the aircraft, as close as 160 m to it. MAL measures with 60 s horizontal integration and 43 m vertical resolution. The volume depolarisation shown in this study is calculated by dividing the measured values for the signal in the depolarisation channel by those from the signal in the parallel-polarisation channel.

2.2.4 Submicron aerosol number concentrations

Aerosol number concentrations were measured with 1 Hz resolution and with 10 % accuracy by two COndensation Particle Counting Systems (COPAS; Curtius et al., 2005; Weigel et al., 2009), each of which consists of two independent Condensation Particle Counter (CPC) channels. The 50 %-detection efficiency size (D_{p50}) for these channels is at particle diameters of 6, 10, and 15 nm (number concentrations denoted as N_6, N_{10}, and N_{15}), respectively, and the fourth CPC channel ($D_{p50} = 10$ nm, N_{10nv}) is preheated to 250 °C in order to evaporate volatile compounds and detect non-volatile residues. The upper size detection limit is largely determined by the sampling inlet, which becomes inefficient for particles with sizes above 1 µm (Weigel et al., 2009). Like the cloud particle probe tips, the aerosol inlets in general might be subject to shattering of cloud particles. The COPAS inlet consists of two sharp-edge diffusers inside each other, providing just a small surface area for impaction of particles (for a detailed description see Weigel et al., 2009). Careful inspection of the data revealed that no shattering events could be identified.

2.2.5 Temperature, humidity, and ozone

Ambient and potential temperature have been measured by the ThermoDynamic Complex (TDC) probe at 1 Hz with an accuracy of 0.5 K (Shur et al., 2007). The navigational system UCSE (Unit for Connection with the Scientific Equipment; Sokolov and Lepuchov, 1998) aboard the Geophysica delivered further relevant parameters as position and true air speed.

The FLuorescent Airborne Stratospheric Hygrometer (FLASH; Khaykin et al., 2009; Sitnikov et al., 2007) was adopted to measure gas phase water, sampling at 1 Hz. The accuracy is 8 % or 0.3 ppmv, and combined with the TDC temperature measurements the uncertainty of relative humidity with respect to ice is 12–17 %.

The Fast OZone ANalyser (FOZAN; Yushkov et al., 1999; Ulanovsky et al., 2001) measured ozone mixing ratios at 1 Hz sampling frequency. It is a chemiluminescence sensor with an accuracy of 10 % and a precision of 0.01 ppm.

3 30 November 2005 – description of the case

A strong Hector storm system developed on 30 November 2005 over the Tiwi Islands north of Darwin, Australia. On this day two research flights were carried out. The first flight

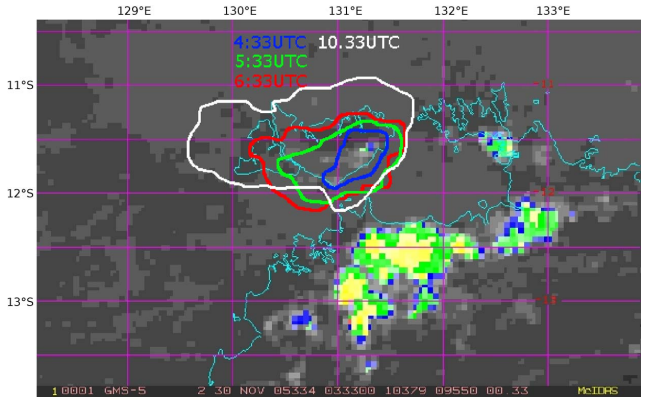

Figure 2. GMS IR cloud top temperature satellite image of the Tiwi Island region. First cloud patches of the developing Hector can be seen. The evolution of Hector is depicted with the coloured contours (see text for explanation). The satellite cloud top temperature colour scale is: > 250 K grey shades, 250–230 K blue shades, 230–210 K green shades, 210–190 K yellow shades, < 190 K red shades.

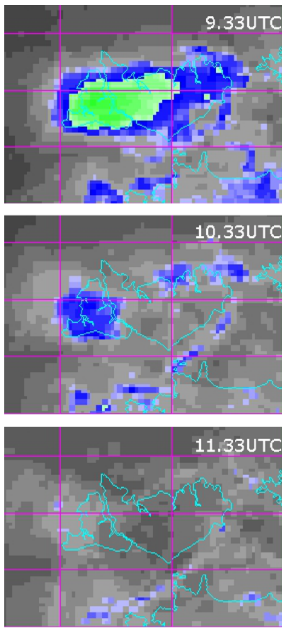

Figure 3. Close-up of GMS IR satellite images of the Tiwi Island region with the dissipating Hector clouds. The colour scale is as in Fig. 2.

(about 13:15 to 17:50 LT, local time = UTC + 9.5 h) probed Hector during its developing and mature stages while the second flight (about 21:40 to 03:00 LT next day) probed Hector in its dissipating stage, with roughly 4.5 h of sampling time inside the upper parts of Hector. Thus, there was only a 4 hour gap between the two flights, which was just enough to service the aircraft and the instruments. Since the Geophysica is flown by one pilot and no additional crew, the instruments run fully automatically and just the pilot changed on the second flight. For reasons of flight safety, the Geophysica did not fly in the convective core itself, but above and around the strong updrafts and downdrafts, i.e. on top of Hector and within the anvil clouds. During the first flight overshooting cloud tops were penetrated in the stratosphere at altitudes up to 18.7 km (Corti et al., 2008; de Reus et al., 2009), with lowest cloud top temperatures below 190 K. The cold point tropopause was situated at around 17.3 km and had a temperature of 185.5 K. The meteorological development of this particular Hector to its mature stage is described in detail by Chemel et al. (2009), making use of cloud resolving modelling, albeit without including information on microphysical properties of the clouds. They used the Advanced Research Weather Research and Forecasting model (WRF; Skamarock et al., 2008) and the Met Office Unified Model (UM; Golding, 1992) with horizontal resolutions of 1 km, and were able to reproduce the overshooting cloud turrets. These overshoots lead to troposphere–stratosphere exchanges, in particular affecting the entry of water vapour in the lower stratosphere. They found a fairly significant moistening above the 380 K isentrope (on average 0.06 ppmv (WRF) / 2.24 ppmv (UM) between 380 and 420 K), while Corti et al. (2008) found positive deviations from measured mean water vapour profiles of up to 1.4 ppmv.

Satellite imagery in the infra-red (IR) for cloud top temperatures is available from the Geostationary Meteorological Satellite 5 (GMS-5), operated by the Japan Meteorological Agency. Figure 2 shows a single GMS satellite image at 13:03 LT where the first cloud patches of Hector can be seen over the Tiwi Islands. The coloured lines show the contours of Hector during its development: blue at 14:03 LT, green at 15:03 LT, and red at 16:03 LT. These contours were fitted to the coloured pixels of the respective satellite images. The white contour gives an estimate of the maximum extension of Hector derived from the satellite image at 20:03 LT, when Hector had already started to dissipate. The figure shows that Hector spread out over the Tiwi islands with its central position remaining stationary during the time span covered by the two Geophysica flights on that day. The dissipation of Hector is depicted in Fig. 3, which shows the satellite images of 19:03, 20:03, and 21:03 LT. While the IR satellite images clearly show the presence of clouds with very high optical thicknesses $\tau \geq 100$ (MTSAT IR NASA LARC cloud product: http://cloudsgate2.larc.nasa.gov/cgi-bin/site/showdoc?docid=22&domain=mtsat&lkdomain=Y) during the first flight on 30 November, the IR satellite images of the second flight show almost no clouds and optical thicknesses are at maximum 2. However, extensive cloud fields have been probed by the aircraft also during the second flight, as apparent from the measurements with the in situ cloud particle instrumentation as well as the backscatter sonde and miniature lidar. The latter clearly shows the existence of ice clouds, inferred from depolarisation measurements,

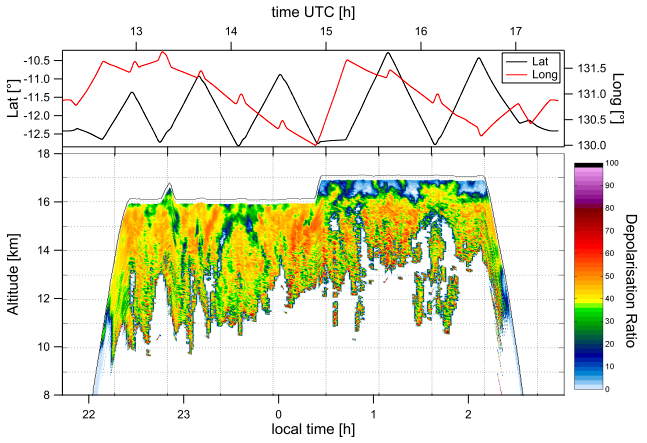

Figure 4. Volume depolarisation ratio measured by the downward looking lidar MAL during the second flight. The remnants of Hector can clearly be seen. The top panel indicates the aircraft's position (latitude and longitude). The lidar detects a surface return at all times (not shown here), thus the cloud layer thickness should be completely captured and well represented. A figure for the first flight is omitted since it is not possible to say whether the layer thickness is adequately presented at all times, due to thick clouds and the laser beam not being able to penetrate through the entire cloud vertical extent. The cloud tops, if not overshooting, were roughly located at about 17 km during the first flight.

as evident from Fig. 4. In those lidar measurements a return from the surface has always been detected, demonstrating the stability of the performance of the MAL instrument. Apparently after the Hector encounter during the first flight, clouds remained in place at around 10–16 km altitude, even though they are not visible in the satellite IR images. Considering the airborne lidar, backscatter, and in situ observations we believe these clouds were not optically thick enough anymore to give sufficient signal for the satellite sensor.

The fact that Hector stayed in place during its development (compare Figs. 2 and 3) leads to the assumption that there was no significant horizontal advection of air during and between the two flights, which could have transported non-Hector clouds or cloud parts into the measurement region. Figure 5 shows the wind fields on the 100 hPa and 200 hPa levels (roughly reflecting flight altitude) on 30 November 2005 at 15:30 and 21:30 LT. Wind speeds around the Tiwi Islands were generally low, so there was no large-scale horizontal transport of air masses on this day. Ten day back trajectories are calculated from ECMWF fields at 0.5° resolution with a kinematic code on a $0.2° \times 0.2°$ 3D box surrounding the flight path, analogously to Law et al. (2010). The closest starting point (in space, time, and height) is attributed to each point of the flight path. These back trajectories, starting along the tracks of the first and second flights, show a general flow from Southeast Asia (Philippines) to the Indian Ocean and then turning towards Australia where they finally reach the Tiwi Islands as a south-westerly flow. In order to identify whether air masses sampled during the second flight were coming from the area of the first flight, 6 hours of synoptic back trajectories originating from the second flight were calculated. These trajectories indicate that the winds between the two flights were weak and air parcels recirculated in the area after being advected to the islands from south-east. A west–east jet was located in the south of the Islands, which did not extend to the measurement region. On the contrary, the area covered by the Geophysica above the Tiwi Islands was located in a relatively quiet zone to the north of the jet.

Furthermore, measurements of ozone mixing ratios have been taken into account in order to check for air mass exchange. Figure 6 shows the observed ozone profiles of the first and second flights. The left-hand side shows the individual data points; the right hand side the median and 33/67 percentiles. The profiles agree well in the middle troposphere (335–350 K potential temperature) while they differ by up to 26 ppbv in the TTL region. This difference can be attributed to upward mixing of low ozone concentrations from the boundary layer (Solomon et al., 2005). This is corroborated by noting from the right panel of Fig. 6 that the same low ozone values (about 40 ppbv at 300 K potential temperature; dark blue) from flight 1 appear during flight 2 between 365 and 375 K (light blue). Air masses in deep convection can be transported from the lower troposphere into the upper troposphere in about 30 min (Thompson et al., 1997). Thus, given the lifetime of ozone in the TTL, a signature of this upward transport can be expected, if no advection of undisturbed air masses from the side takes place. The higher ozone values of the data points enclosed by the orange ellipse were sampled in cloud-free air and at the cloud edge upwind of the Hector anvil and its convective core. Thus, the ozone reduction due to upward transport of low-level air did not take place here, also keeping in mind that the flow was coming from the east. It also shows that horizontal air mass advection was negligible. Additionally considering the satellite images and trajectories for the two flights on 30 November, it seems reasonable to assume that the same clouds have been probed at different times and that there had been no recent horizontal advection of other clouds into the sampling region.

4 Microphysical evolution of Hector

4.1 Observations of ice particles in Hector development stages

During the two flights, clouds were penetrated by the aircraft and a set of size distributions was measured. The cloud measurements of both flights were collected and separated into the following groups: developing, overshoots, mature, and dissipating stages. Measurements obtained between take-off of the first flight (13:14 LT) and 14:17 LT are classified as developing stage. Between 14:17 and 16:30 LT clouds have been probed in convective overshooting regions in the strato-

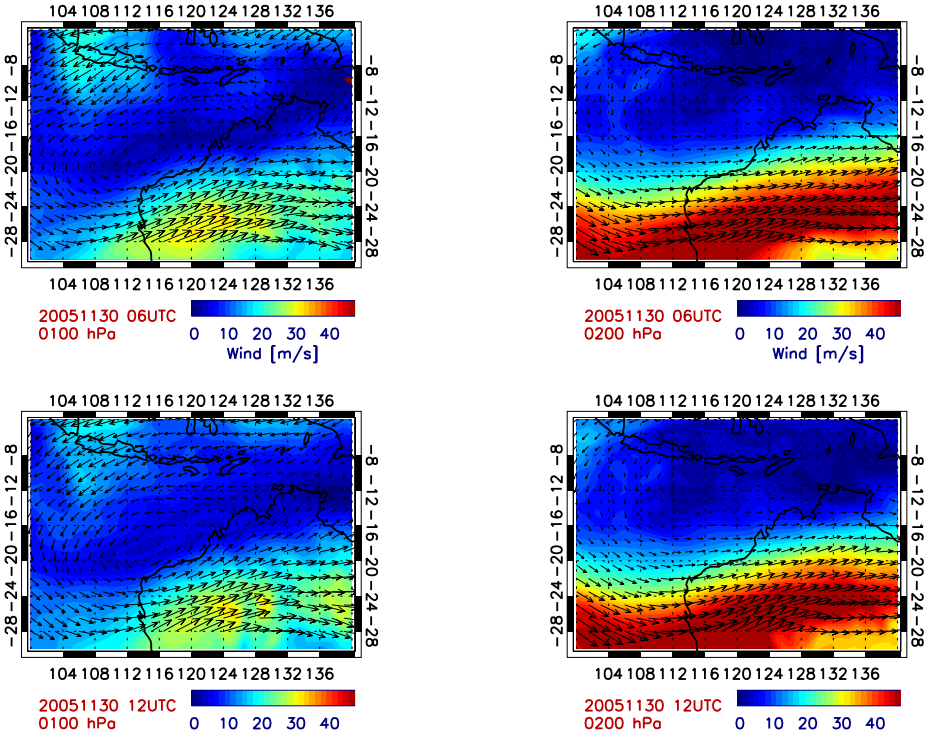

Figure 5. Wind fields from ECMWF at 100 hPa (left panels) and 200 hPa (right panels) at 15:30 LT (upper panels) and 21:30 LT (lower panels).

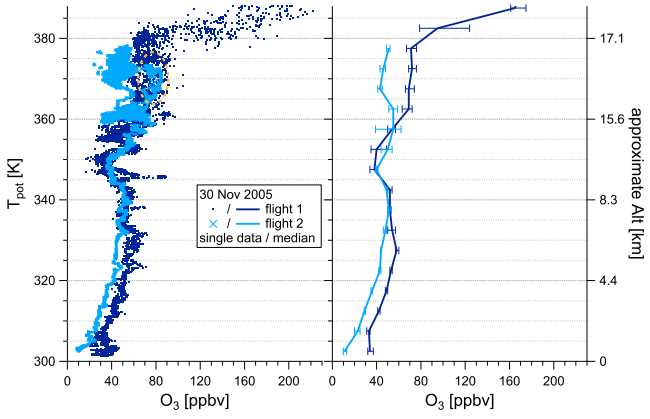

Figure 6. Profiles of ozone mixing ratios from first and second flight on 30 November 2005. Individual (1 Hz) data points are shown in the left panel, median and 33/67 percentiles in the right panel. The orange ellipse encloses data points that were recorded at the beginning of the second flight at the eastern edge of the flight path. The number of these points is much lower than those at later times of the flight, thus these observations have no visible effect on the median as shown in the right panel.

sphere. The analyses of these measurements are described in detail by de Reus et al. (2009) and Corti et al. (2008) and are not further considered here, because of their focus on higher altitudes. Observations from 16:30 LT to landing (17:48 LT) are classified as mature. All measurements from the second flight (21:49–02:51 LT) fall into the dissipating stage (however, cloud particle data were analysed only until 01:00 LT, due to an FSSP-100 power failure afterwards). The dissipating stage cloud data have further been checked and filtered for possible influence of non-Hector clouds on the southern flight part, according to the 6 h back trajectories on the flight path of the second flight. When the trajectories indicated a possible influence of a non-Hector cloud, the data were excluded from the analysis. Due to this filter criterion, about one third of the size distributions in the dissipating stage have been excluded from further analysis.

4.1.1 Size distributions

The Hector size distributions are classified into altitude bins of 5 K potential temperature. The vertical profile, in terms of potential temperature, of the averages of every Hector stage is shown in Fig. 7. Most size distributions are averaged over a sample time period of 20–25 s (corresponding to roughly 3–5 km flight path); in the case of small number concentrations this averaging time is extended to up to 145 s (about 25 km flight distance) in order to obtain better sampling statistics. The numbers (#) of compiled size distributions per class and potential temperature bin are given in Table 1 together with mean values for ice water content (IWC), number concentrations (N), effective radius (r_{eff}), relative humidity with re-

Table 1. Averages of microphysical and meteorological properties for the different Hector stages and altitude bins as in Fig. 7: ice water content (IWC), cloud particle number concentration (N), effective radius (r_{eff}), relative humidity with respect to ice (RHi), and ambient temperature (T). The last column indicates the number of size distributions for each class.

T_{pot} [K]	case	IWC [10^{-3} g m^{-3}]	N [cm^{-3}]	r_{eff} [µm]	RHi [%]	T [K]	#
350–355	dev	0.21	0.02	21.8	–	199.3	1
	mat	4.44	0.30	74.5	83	200.4	6
	dis	2.78	0.20	36.6	72*	205.6	6
355–360	dev	0.21	0.03	16.8	–	195.0	27
	mat	4.73	0.44	41.6	95	195.1	19
	dis	0.27	0.14	14.9	105	195.5	10
360–365	dev	0.04	0.02	9.1	–	189.2	3
	mat	3.12	0.45	14.9	100	189.7	4
	dis	0.08	0.05	10.2	91	192.0	100
365–370	dev	0.03	0.06	5.7	–	186.9	2
	mat	0.16	0.07	14.1	105	188.7	5
	dis	0.03	0.02	8.6	110	187.2	1
370–375	dev	0.002	0.007	3.2	–	186.0	1
	mat	0.016	0.009	5.9	113	187.6	3
	dis	0.008	0.008	5.1	101	188.1	3

* RHi measurements available only for five size distributions.

spect to ice (RHi), and ambient temperature (T). In three classes only one size distribution has been measured. This is indicated by dashed instead of solid lines in Fig. 7. The general findings from Fig. 7 and Table 1 are as follows.

- The size distributions show a decrease in number concentrations and particle size with increasing altitude. This has also been observed by Frey et al. (2011) and de Reus et al. (2009). The only exception is the developing case that exhibits clearly higher number concentrations in the 365–370 K bin, contrary to the general decrease in number concentrations with altitude.

- The mature stage exhibits the largest number concentrations and sizes, as expected, while the smallest particle sizes and concentrations can be found for the developing Hector cases. Exception: in the 365–370 K-bin number concentrations for the small particles are largest for the developing stage.

- Table 1 shows that the mature stages exhibit the largest values for the microphysical parameters in each altitude bin, followed by the dissipating stage, with the developing stage having the smallest values. There are two exceptions: in the 355–360 K bin the effective radius of the developing Hector stage is slightly larger than the dissipating stage and in the 365–370 K bin the developing stage has higher number concentrations than the dissipating stage that are almost as high as those for the mature stage.

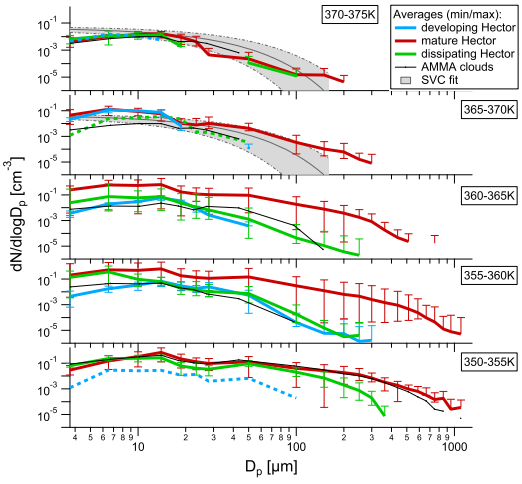

Figure 7. Vertical profile of cloud particles' size distributions. The averages of the respective Hector development stage (developing, mature, and dissipating) for every potential temperature bin of 5 K are given. A dashed line denotes that only one size distribution for the respective Hector class had been measured in the corresponding altitude bin. Vertical bars show the position of the minimum and maximum distribution for the respective average. Further parameters can be found in Table 1. Additionally, the mean size distributions of measurements inside MCS anvil outflow during African Monsoon Multidisciplinary Analysis (AMMA) and a fit for SVC are displayed.

- The ambient temperature became warmer with increasing age of Hector. (The only exception here is the dissipating Hector stage in the 365–370 K bin; however, only one size distribution is given here, which was sampled over 60 s.)
- The RHi in the mature and dissipating stages is generally close to saturation, considering the measurement uncertainty (12–17 %). The rather low RHi in the 350–355 K level of the mature stage could possibly be explained by entrainment of dry air from the side of the cloud. Supersaturation in ice clouds will not be removed immediately, but RHi of up to 200 % have been found in cirrus (Krämer et al., 2009; Spichtinger and Krämer, 2013). In the dissipating stage ice particles sediment out of the cloud, which does not affect RHi in the first instance. Higher temperatures in the dissipating cloud decrease RHi at first but when reaching subsaturation ice crystals will evaporate and, thus, an RHi around saturation would be expected.
- In the highest altitude bin the size distributions for all cases are fairly similar, only differing in the sizes of the largest detected particles.

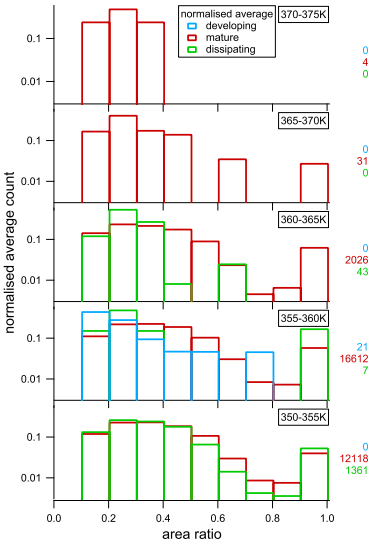

Figure 8. Vertical profile of area ratio histograms. The histograms are normalised to a total value of 1 (each bin divided by the total number of counts) to make their shapes comparable. The coloured numbers at the right hand side indicate the number of particle images considered in this analysis.

4.1.2 Cloud particle shapes

In the following the area ratio is used to provide information about how particle shapes change according to the size distributions in Fig. 7. The area ratio is defined as the shaded area in the particle images divided by the area of a circumscribing circle with the maximum dimension as diameter. Particles with a maximum dimension smaller than 5 pixels (i.e. 125 µm) were excluded from this analysis, because they are too small to give reasonable shape information. This limits the number of available particles for the area ratio analysis. From the remaining data, histograms have been derived for each potential temperature bin. The histograms alongside the number of considered particles are shown in Fig. 8. Particles with area ratios smaller than 0.1 were excluded as a general correction to remove artefacts such as streakers. Few particles are left for evaluation in the developing stage, all in the 355–360 K bin. The histogram indicates an increasing contribution of particles with small area ratios, i.e. more elongated particles. However, the meaningfulness of this has to be viewed with caution due to the small sample size. The mature stages show a bimodality, peaking at 0.2–0.4 (probably chain aggregates or column particles), and a second peak at 0.9–1 (possibly aggregates or rimed particles). The dissipating stage looks similar to the mature stage, though the bimodality disappears higher up. If the second peak was due to aggregates and rimed crystals these would certainly have been big and already sedimented. Note that even though the normalised area ratio histograms for mature and dissipating Hector look similar, the number of particles in those two classes is different. However, the similarity of these two stages indicates that the dissipating clouds are remnants of the mature stage.

4.2 Comparison with data from West African MCS

The black lines in Fig. 7 show the median size distributions of clouds measured in the vicinity of West African MCS during the SCOUT-AMMA campaign (Frey et al., 2011) for comparison. These MCS are correlated to African easterly waves and further triggered by topographic features (Mekonnen et al., 2006). Note that the median size distributions for the MCS clouds include clouds of all development stages. However, a comparison is useful, especially given the scarcity of data on high-altitude deep convective clouds. In general, the AMMA MCS clouds are very different from Hector clouds regarding (a) the meteorological mechanisms and the aerosol reservoirs behind their respective formation, (b) the different surface conditions, (c) their largely different sizes, extents, and temporal evolutions, (d) the much longer lifetimes of the AMMA clouds, and many other aspects connected with their propagation/movement and precipitation. However, in terms of their impact on the TTL, it seems that the effects, as seen from the local in situ measurements, of the two cloud types are quite similar. The size distributions in the respective potential temperature bins are not very different, and also at the lower altitudes (350–355 K) in the anvil region the number concentrations are alike over the covered size range. Only in the altitude range from 355 to 370 K the mature stage exhibits much larger and more cloud particles than the AMMA clouds. Since the observed Hector is very strong it may eas-

ily exceed the median AMMA cloud, which also includes aged clouds (about 10 h old), in terms of particle sizes and numbers. This also shows the potential of Hector for delivering large amounts of IWC into the TTL. The developing and dissipating stages compare fairly well to the AMMA clouds with only small differences: (a) in the 355–360 K range the AMMA cloud particles have a smaller maximum diameter (up to 100 µm compared to 300 µm/250 µm); (b) in the 360–365 K bin the developing Hector has smaller ice crystals than the AMMA clouds, while the dissipating Hector shows a larger amount of small particles than the AMMA clouds; (c) in the 365–370 K range the dissipating Hector compares well to the AMMA clouds, while the developing Hector has more than an order of magnitude more smaller particles. However, generally, these very different deep convective systems show rather similar size distributions in the TTL, with Hector having slightly larger particles.

4.3 Potential for SVC generation

One possible formation pathway for SVC (Thomas et al., 2002; Davis et al., 2010; Frey et al., 2011) is as remnants of deep convection (e.g. Massie et al., 2002; McFarquhar et al., 2000). For example, McFarquhar et al. (2000) found that almost 40 % of SVC occurred in an area where there was convection in the previous 12 h. For this reason, the upper two potential temperature bins of Fig. 7, which are typical for SVC, include a fit function for SVC that Frey et al. (2011) derived by combining all SVC measurements reported in the literature until then. The grey shading denotes the standard deviation from the fit function. The Hector size distributions show a similarity to the SVC distribution. Particularly the size distributions of the dissipating stage compare quite well to this SVC fit, exhibiting similar sizes and number concentrations. However, it can be excluded that the clouds in the different Hector stages are SVC: the developing and mature cases are directly linked to the convective storm and are also optically too thick, as can clearly be inferred from satellite images. Furthermore, the mature stage shows larger particles than have been observed in SVC. Additionally, together with the developing stage, the mature stage exhibits higher numbers of small particles (around 10 µm) in the 365–370 K bin. The clouds in the dissipating stage have a geometrical thickness that is much larger than that of a typical SVC, i.e. more than 6 km vertical extension compared to less than 1 km for SVC. However, this comparison and the similarity show that the dissipating Hector might be a precursor for SVC. The transformation may happen in different ways: the upper cloud part may persist while the lower cloud parts diminish due to precipitation of the ice crystals or complete sublimation. In another scenario wind shear may split the cloud into thin layers (Jensen et al., 1996) and thus transform parts of the dissipating cloud layer into SVC. The lidar measurements in Fig. 4 suggest that the dissipating cloud layer becomes thinner in vertical extension by disappearance of the lowest cloud parts. This may be a first hint for transformation towards an SVC. In case of full decay of the dissipating cloud by partial or complete sublimation of the ice, it will leave behind a layer of humidified air in the TTL which might be favourable for SVC formation at a later time. Even if not dissipating further and/or transforming into an SVC, the cloud may take up more humidity, causing ice particles to grow, sediment, and dehydrate the air. Since air in this region is subject to slow upwelling, changes in humidity here impact the stratospheric humidity.

The optical thickness (τ) for the cloud below the aircraft in Fig. 4 is retrieved from the two lidar signals I_1 and I_2 after both signals are corrected for optical background noise and detector dark noise. I_1 is the signal from the sea surface while I_2 is the backscatter signal from the reference layer near cloud top (as seen by the aircraft, starting from 300 m below the aircraft). From the standard lidar equation (Measures, 1984), the optical thickness of the atmosphere below the aircraft (cloud and molecular atmosphere contributions) is given by:

$$\tau_{\text{total}} = 0.5 \ln\left(\frac{I_2}{I_1}\frac{a}{\beta\, dz}\left(\frac{R_{\text{cl}}}{R_{\text{sea}}}\right)^2\right), \quad (1)$$

where R_{sea} is the distance from the aircraft to the sea level, R_{cl} the distance from the aircraft to the cloud top layer (i.e. 300 m), a the sea albedo, β the total backscatter coefficient of the cloud top reference layer, and dz the lidar resolution. The cloud optical thickness τ_{cloud} is then obtained by subtracting the optical thickness of the molecular atmosphere (τ_{mol}) between the cloud top reference layer and sea from τ_{total}:

$$\tau_{\text{cloud}} = \tau_{\text{total}} - \tau_{\text{mol}}. \quad (2)$$

Considering errors on albedo, cloud reference layer backscatter coefficient, and signal ratio cloud top/sea surface (e.g. due to changing albedo and variations of the cloud top signal), the retrieved cloud optical thickness of the dissipating clouds is 0.88 ± 0.44. Since this calculation includes the whole atmosphere between aircraft and sea surface, some effects of evaporation may lead to larger values of τ. Furthermore, the correction for the molecular atmosphere was performed for dry and not for wet atmosphere, so likely τ_{mol} is slightly underestimated. Thus, the value obtained from MAL observations represents an upper limit of τ_{cloud}.

Following Garrett et al. (2003), a rough estimate about the optical thickness can be obtained for the upper cloud layer also from the measurements of the cloud microphysics probes:

$$\tau = \Delta z\, \beta_{\text{ext}} = \Delta z\, \frac{3\text{CWC}}{2\rho\, r_{\text{eff}}}, \quad (3)$$

where Δz is the cloud layer thickness, β_{ext} the extinction coefficient, CWC condensed water content, ρ the density of ice, and r_{eff} the effective radius. Given the ambient temperatures,

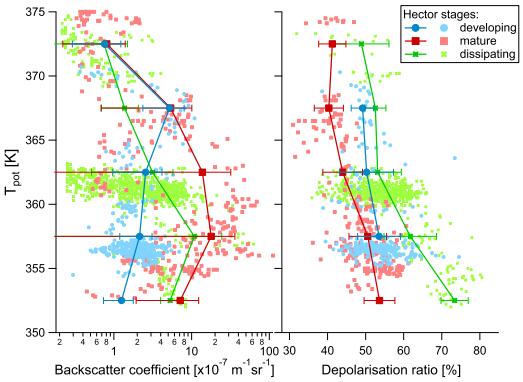

Figure 9. MAS cloud particle backscatter coefficient (left) and cloud particle depolarisation ratio (right). The light coloured markers indicate the individual measurements. Lines and markers represent the averages for the 5 K altitude bins as in Fig. 7, with error bars denoting the standard deviation.

the CWC equals the IWC. Using the measured variables, the optical thickness calculations reveal that a layer as thick as 1 km (which is rather thick for an SVC) can be classified as thin cirrus or SVC, with values of τ ranging from 6×10^{-5} to 0.2. Given that the MAL τ_{cloud}-retrieval considers an up to 6 times as thick cloud layer, where larger particles might be present in the lower levels (cf. non-uniform depolarisation in Fig. 4), these two retrievals are in reasonable agreement. When extrapolating the observed IWCs and r_{eff} to a 6 km thick cloud layer, the optical depths retrieved from the in situ particle probes are 3.6×10^{-4} to 1.2. Compared to optical thicknesses of deep convective anvil clouds (cf. Kwajalein measurements of τ between 20 and 40; Heymsfield, 2003), the observations here show the transition to thin or subvisible clouds.

5 Backscatter and aerosol measurements and their implications for freezing history

5.1 Backscatter sonde observations

The optical measurements by MAS are used to obtain more information about the clouds and their structure. Figure 9 shows profiles of cloud particle backscatter coefficient and cloud particle depolarisation for the cloud cases and bins as in Fig. 7. Only in-cloud data are presented.

5.1.1 Backscatter coefficient

The cloud particle backscatter coefficient on the left demonstrates that the largest backscattering occurs in the mature stages of the cloud while the smallest occur in the developing stages, as would be expected. The altitude of the maximum of the backscattering on the profiles descends as time evolves. The maximum in the developing/mature/dissipating stage lies in the 365–370 K/355–365 K/355–360 K bins, respectively. This behaviour coincides with the observed distributions of cloud particle surface density (as derived from the particle probe observations but not shown here) and with the maxima seen in the size distribution plot in the smaller ice particle size range (up to about 20 µm) for each development class.

5.1.2 Freezing history revealed from depolarisation ratio

The cloud particle depolarisation (right panel) is more or less constant in the developing stage and decreasing with altitude for the mature and dissipating stages. This indicates that glaciation had already taken place before the observations in the developing stage (all cases at ambient temperatures < 200 K), which, judging from the satellite pictures, was in its first hour of development. Heymsfield et al. (2005, 2009) showed that in convective cells with strong updrafts supercooled cloud droplets may reach the homogeneous nucleation level (at about $-38\,^{\circ}$C) and rapidly freeze there. However, they might also freeze heterogeneously at lower altitudes. Subsequently, the newly frozen particles are transported in the strong updrafts from the mixed-phase region into the measurement region without much riming. Therefore, particles with similar shapes can be found in the upper cloud parts, which might be a tentative explanation for the absence of altitude variation of depolarisation in the developing stage. Not all particles necessarily reach the measurement region: some may escape in the turbulent environment before reaching higher altitudes. On their way up, the crystals may further grow by deposition, which leads to a broadening of the size distributions. As a second possibility, homogeneous freezing of particles at $T < -38\,^{\circ}$C from solution droplets on top of Hector cannot be ruled out completely. This should also lead to ice particles with similar depolarisation, due to the narrow band of conditions under which the freezing would happen. However, such in situ formed particles would be expected to have sizes of only up to a few tens of µm (e.g. Gallagher et al., 2012), whereas sizes in the developing stage exceed 100 µm. In the mature stage also larger particles reach the upper parts of the cloud. Those larger ice particles are a result of riming and aggregation in the mixed phase part of the cloud at lower levels, or aggregation due to electrical charges also in the upper cloud parts (Stith et al., 2004). Examples of these larger ice particles are shown in Fig. 10. The decreasing levels of depolarisation with altitude for the mature and dissipating Hector case reflects a change in the average morphology of the particles. The exact reasons for this are a matter of speculation: particles formed by riming and accretion grow to larger sizes which will first be removed from the upper cloud parts and later also from the lower cloud parts by sedimentation and precipitation. Additionally, fewer large particles might be transported into the higher cloud layers. Thus, different shapes in the upper cloud

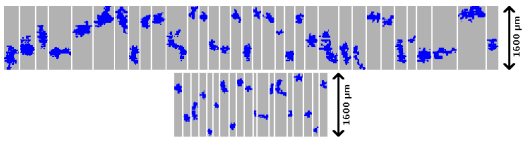

Figure 10. Images taken by the CIP during the mature (upper) and dissipating (lower panel) Hector phase. No developing Hector images are shown since these were only a few pixels and no shapes can be inferred from them.

layers can be expected, and with them different depolarisation ratios. In general, for a given shape the depolarisation ratio increases with the dimension of the particle (i.e. within the range of dimensions not far from the wavelength) up to an asymptotic value, which depends only on shape (Liu and Mishchenko, 2001). In the case of cloud particle observations here, the measurements are in the asymptotic range. Hence, the depolarisation ratio will not increase with increasing cloud particle size. The precise functional relationship between the asymptotic value and shape is yet unknown. For example, plates and spheroids produce similar depolarisation ratios, while columns attain higher values (e.g. Noel et al., 2004). However, when a change in the depolarisation ratio of a probed cloud particle population is detected, it can be concluded that the average morphology of the cloud particle population changes as well, as is the case here. In the absence of good methods for the in situ detection of accretion and riming in the turbulent parts of Cb clouds, the statements in this subsection remain speculative. Detailed numerical simulations of the cloud processes are needed for clarification. The same applies to the influence of rimed particles of various sizes on the detectable depolarisation, which could be simulated in a sensitivity study.

5.1.3 In situ ice particle nucleation in aged anvil

As the analysis of area ratio (cf. Fig. 8) shows, there is a great similarity between the mature and dissipating Hector cloud. Thus, it might be indicative that these crystals (> 125 µm) are ageing crystals from the mature stage. However, the small ice particles are not included in this analysis and the depolarisation of the dissipating stage is quite different to that of the mature clouds. This might be a hint for in situ nucleation of ice particles at this altitude, similar to the nucleation of new ice as observed in deep convection at the cloud edge by Gallagher et al. (2012). In that case, the smaller ice particles, or a subset of them, would be recently frozen in situ while the larger crystals are leftovers from the mature stage. However, the measurements in Table 1 show a more or less saturated environment, which would not support nucleation unless some nucleation had occurred prior to the measurement in a then supersaturated environment.

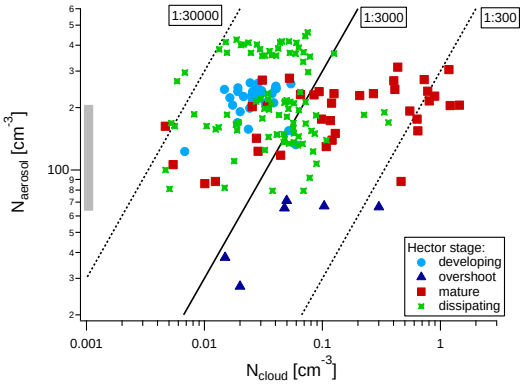

Figure 11. Activation of aerosol to cloud particles estimated by the number concentrations of aerosol and cloud particles. Each point corresponds to one size distribution in Fig. 7, with the same colour code. The overshooting Hector cases were observed at potential temperatures of 386–414 K. The grey bar on the left denotes in-cloud aerosol concentrations observed on other flights during SCOUT-O3. The size ranges are 2.7 to 1600 µm for the cloud particles and larger 15 nm for the aerosol particles (up to approximately 1 µm). See text for further explanation.

5.2 Cloud to aerosol particle ratio

In order to shed light on aerosol–cloud interactions, and possibly gaining information about the freezing history of the cloud, one can look at the correlation between aerosol and cloud particle number concentrations. Furthermore, assuming that aerosol and cloud particles are transported with the same efficiency in the convective updrafts, this relation can also be used to estimate how effectively aerosol particles are activated to cloud particles. In this regard, the cloud particle number concentrations would be used as a proxy for the residual aerosol (i.e. activated aerosol) particles, while the COPAS N_{15} measurements represent a proxy for the interstitial aerosol. Since the sampling efficiency η of the COPAS inlet sharply decreases for particles larger than 1 µm (i.e. η is about 100 % for $D_p \leq 1$ µm but ranges below 30 % for $D_p > 3$ µm) and aerosol number concentrations are much larger than the cloud number concentrations, the contribution of possibly counted cloud particles in the COPAS system is negligible. In the anvil region (i.e. outside the main updrafts and downdrafts), where the measurements were obtained, cloud ageing effects as the release of submicron aerosol by particle sublimation or losses of aerosol particles onto ice surfaces might apply to this estimate. Figure 11 shows the aerosol number concentrations vs. cloud particle number concentrations for the selected Hector cases. $N_{aerosol}$ refers to the COPAS N_{15} measurements in most cases; in some of the dissipating Hector cases N_{10} have been used instead, since N_{15} measurements were not available. However, cloud segments where new particle formation events occurred (as observed by Weigel et al., 2011) were identified and excluded from the analysis here. New particle formation events are

Table 2. Averages of activation ratio estimate and aerosol number concentrations for the different Hector stages and altitude bins as in Fig. 7. Note that aerosol measurements are not available for all given size distributions.

T_{pot} [K]	Case	Activation ratio $\times 10^{-4}$	$N_{aerosol}$ [cm^{-3}]
350–355	dev	1.05	191
	mat	20.29	238
	dis	no $N_{aerosol}$	no $N_{aerosol}$
355–360	dev	1.24	233
	mat	11.99	226
	dis	8.22	199
360–365	dev	1.26	182
	mat	30.15	151
	dis	2.35	248
365–370	dev	3.91	144
	mat	4.99	130
	dis	1.61	110
370–375	dev	0.55	123
	mat	1.03	93
	dis	0.97	88

not thought to enhance the N_{15} significantly since the newly formed particles are smaller than 15 nm. The coloured symbols represent the different Hector stages: light blue dots represent developing stage, mature cases are depicted by red squares, overshooting cases are shown in dark blue triangles, and the dissipating stage of Hector is displayed by green stars. Figure 11 additionally shows some correlation lines, e.g. the 1 : 3000 line denotes where one out of 3000 aerosol particles would be activated to a cloud particle, under the abovementioned assumptions.

5.2.1 Developing stage

The developing cases all group very closely together, although the data were recorded at very different altitudes. Additionally, the developing Hector cases have in general the smallest cloud to aerosol particle ratio compared to the other cases. This is also obvious in Table 2, which summarises the averages for activation ratio estimate and aerosol number concentrations. The fast updrafts in the developing stage of Hector may lead to rapid glaciation of supercooled water (e.g. observed in Keenan et al., 1994; Heymsfield et al., 2005). Thus, the grouping of the data points and the rather low cloud to aerosol particle ratio (less activated aerosol) can be an indication of homogeneous freezing/rapid glaciation in such updraft. Also the depolarisation ratio profile in Fig. 9 suggested glaciation under very similar conditions. Together these findings suggest that the developing cloud parts were formed under very similar conditions and with a similar history of freezing within a short time. There is one outlier in the developing Hector cases with lower aerosol and cloud particle concentrations, which corresponds to the size distribution in the highest altitude bin. Possibly the updraft was weakened when reaching this altitude, and thus not transporting as many of the newly frozen small cloud particles as to the other altitudes.

5.2.2 Mature stage

In comparison with the developing stage, the samples from the mature Hector cases are characterised by a similar quantity of aerosol particles, but a much higher quantity of cloud particles. This leads to the highest cloud to aerosol particle ratios among all stages of cloud evolution. These higher ratios could either be an effect of different freezing mechanisms, e.g. involving contact freezing, or occur due to washout effects. At this time the cloud particles have experienced microphysical processes such as riming and aggregation, thus larger ice particles were formed as growth by diffusion plays a minor role for growing particles to those sizes. Examples for recorded particle images of such rimed and aggregated particles are shown in Fig. 10. These larger particles are important for efficient ice multiplication by ice–ice collision, as detailed below. The change in ice particle numbers is reflected in the size distributions in Fig. 7, showing an increase in the total particle number, as well as in the higher backscatter depicted in Fig. 9. Ice multiplication processes might be the reason for higher cloud particle concentrations while aerosol concentrations stay fairly similar to those of the developing Hector cases. Collisions of ice crystals involving rimed crystals can lead to mechanical breakup of the particles, leading to significantly higher number concentrations also at temperatures lower than during the Hallett–Mossop process (Vardiman, 1978; Yano and Phillips, 2011). These multiplication processes could also have happened in the lower parts of the cloud, with secondary ice crystals subsequently carried upwards into the measurement region. There are some outliers on the side of lower aerosol and cloud particle concentrations in the mature stage too, which correspond to size distributions in the higher altitude bins.

5.2.3 Dissipating stage

Compared to the other Hector stages, the dissipating cases show the largest spread in the data points. This might be an effect of ageing of the clouds, whereby in the course of time aerosol particles are collected on the cloud particle surfaces but on the other side might be released when cloud ice particles (partly) evaporate. Examples of particle images for the dissipating stage are also given in Fig. 10. The cloud to aerosol particle ratios decrease from the mature to the dissipating stage. These again lower ratios could be explained by evaporation and subsequent release of ice nuclei and other aerosol particles which had been collected onto the cloud particle surface. Even though events of new particle formation have been excluded from the analysis, it cannot be ruled out completely that during such events particles have already

grown to sizes larger than 15 nm. Those particles could deliver an additional source for aerosol particles that reduce the cloud to aerosol particle ratio. However, such effects were very local and could, as an estimate, extend over about 5 km.

5.2.4 Overshooting events

To complete the picture, the overshooting events are displayed in Fig. 11 as well. They exhibit fairly high cloud particle concentrations but less aerosol than the developing and mature cases. In these cases aerosol number concentrations are higher than the stratospheric background (on this day 20–40 cm^{-3} as measured by COPAS) and are comparable to upper tropospheric values. This is an indication that not only cloud particles but also aerosol particles were transported upwards into the stratosphere by the overshooting convection.

In general, there is a decrease in cloud to aerosol particle ratio with altitude in the mature and dissipating Hector stages while the ratio is fairly constant in the developing stage (see Table 2). There are two exceptions for the cloud particle number concentration maxima in the developing case (365–370 K) and mature case (360–365 K). Without detailed numerical simulations of the cloud microphysical and dynamical processes, which produce the corresponding output variables, the reasons for the observed ratios remain speculative.

Using aerosol number concentrations that were observed by Allen et al. (2008) in background boundary layer conditions, Connolly et al. (2013) have shown that the observed Hector storm systems were indeed influenced by those concentrations. By taking the number concentrations into account the simulations were mostly improved, for example by changing the formation and strength of Hector. Since the data presented here were obtained in the TTL region, they cannot be used for model initialisation. However, they can be used for model evaluation and testing the robustness of the treatment of aerosol–cloud interactions in the cloud microphysics schemes. For these reasons our data here complement the measurements of Allen et al. (2008). Finally, we analysed the vertical profiles of the submicron aerosol number density and their non-volatile fraction. Above the 355 K level N_{10} were close to the regional background concentrations outside of the clouds and about 35 to 50% of the particles contained non-volatile cores (Borrmann et al., 2010). For the lower parts no differences were found between the two flights. Apparently, these variables were not measurably influenced by Hector.

6 Conclusions

This case study presents in situ measurements of cloud microphysical properties of a Hector thunderstorm. Due to the double flights it was possible to obtain measurements throughout a large part of the life cycle of Hector. This gave us a unique opportunity to classify the size distributions in terms of cloud development stages, a net advantage with respect to other studies that looked at size distributions in tropical deep convective clouds (e.g. McFarquhar and Heymsfield, 1997; de Reus et al., 2009). Most experimental as well as modelling work has focused on the developing and mature stages of Hector but not on its dissipating stage. However, as shown here, the dissipating stage exhibits a vertically extensive cloud layer of roughly 6 km, spread out through the TTL, which is not negligible in terms of TTL humidity and ultimately stratospheric humidity.

The data are classified into developing, mature, and dissipating stages and additionally into altitude bins of 5 K potential temperature. The evolution of the particle properties with time and altitude is shown. The developing stage exhibits rather small ice particles (maximum size 300 µm) compared to the later development stages. Maximum particle sizes are seen in the mature cases (larger than 1 mm), potentially exceeding sizes of continental tropical convection. Furthermore, the mature stage exhibits the largest number concentrations as well as ice water content and effective radii. The developing cases show the lowest number concentrations and ice water contents and smallest effective radii, except in the altitude between 365 and 370 K, where number concentrations and effective radii exceed those of the dissipating stages. The values for the microphysical parameters are summarised in Table 1.

The development of the Hector clouds is also obvious in the aerosol to cloud particle ratio. Furthermore, it gives indications of a change in freezing mechanisms with increasing lifetime of Hector: the developing Hector shows very similar cloud to aerosol particle ratios and cloud particle morphology, indicating a rapid freezing under similar conditions. The mature Hector cases show rimed ice crystals and (chain) aggregates, and higher cloud to aerosol particle ratios, thus a change to riming and aggregation. In the dissipating stage Hector shows a wide variety of cloud to aerosol particle ratios, which might be an effect of ageing. Furthermore, according to the area ratio analysis the cloud particles have similar shapes to the particles in the mature stage, also indicating ageing. However, the depolarisation ratios of the dissipating and mature stages differ. Thus, it is valid to speculate that small ice crystals may have nucleated in situ in the ageing cloud. These results show that cloud to aerosol particle ratio varies with the development stage of the convective cloud system and thus the cloud's development stage has to be taken into account in aerosol–cloud interaction studies. Concerning the influence of Hector on the TTL region a fingerprint in the ozone profile was identified, while no differ-

ences were found in the profile measurements of the submicron aerosol concentrations and the non-volatile fraction of these concentrations between the two flights above the 355 K potential temperature layer.

In the dissipating stage Hector consists of a persistent and vertically extensive cloud layer that is optically thin and has further characteristics similar to those of SVC. The persistent cloud layer may either lead to humidification of the TTL due to evaporation of ice crystals or by growth and sedimentation lead to dehydration of the TTL. Thus, this layer certainly has non-negligible effects on radiation and water vapour content. Furthermore, the dissipating stage could act as a precursor for SVC formation: shear flows may transform parts of this cloud layer into SVC or, in case of sublimation of the cloud, conditions for in situ formation of SVC may be provided. Further detailed model analyses are required to provide estimations for the (de)hydrating effect. In any case, these observations show that the dissipating stage of a deep convective system imposes some importance regarding TTL humidity.

The data presented in this study provide a contribution to the very sparse in situ data set of TTL convective cirrus, including a classification of the cloud system's development stage. Though it consists of only one case study, this work shows the variability in TTL convective cirrus microphysics with lifetime.

Acknowledgements. We thank Sebastian Raupach, Christian von Glahn, and Hermann Vössing from the University of Mainz for preparation of the CIP and FSSP instruments and collection of data during the SCOUT-O3 campaign. Special thanks to the entire Geophysica crew and the local authorities in Darwin for their excellent collaboration during the campaign. The SCOUT-O3 project was funded by the European Commission (GOCE-CT-2004-505390) and additional financial support was provided by the Max Planck Society and the Collaborative Research Centre "The Tropospheric Ice Phase" (SFB-641). W. Frey is supported by the DFG Research Fellowship "Tropical High Altitude Clouds and their Impact on Stratospheric Humidity" (FR 3325/1-1). The work is supported in part by the Australian Research Council (ARC) Centre of Excellence for Climate System Science (CE110001028). S. Borrmann is supported in part by the European Research Council (Seventh Framework Program) through the ERC Advanced Grant Agreement No. 321040 (EXCATRO). We thank Darrel Baumgardner and two anonymous referees for their valuable comments, which greatly improved the paper.

The service charges for this open access publication have been covered by the Max Planck Society.

Edited by: T. Garrett

References

Allen, G., Vaughan, G., Bower, K. N., Williams, P. I., Crosier, J., Flynn, M., Connolly, P., Hamilton, J. F., Lee, J. D., Saxton, J. E., Watson, N. M., Gallagher, M., Coe, H., Allan, J., Choularton, T. W., and Lewis, A. C.: Aerosol and trace-gas measurements in the Darwin area during the wet season, J. Geophys. Res., 113, D06306, doi:10.1029/2007JD008706, 2008.

Baker, B. and Lawson, R. P.: Improvement in Determination of Ice Water Content from Two-Dimensional Particle Imagery. Part I: Image-to-Mass Relationships, J. Appl. Meteorol. Clim., 45, 1282–1290, doi:10.1175/JAM2398.1, 2006.

Baker, M. B.: Cloud microphysics and climate, Science, 276, 1072–1078, doi:10.1126/science.276.5315.1072, 1997.

Baker, M. B. and Peter, T.: Small-scale cloud processes and climate, Nature, 451, 299–300, doi:10.1038/nature06594, 2008.

Baumgardner, D., Dye, J. E., Gandrud, B. W., and Knollenberg, R. G.: Interpretation Of Measurements Made By The Forward Scattering Spectrometer Probe (FSSP-300) During The Airborne Arctic Stratospheric Expedition, J. Geophys. Res. - Atmos., 97, 8035–8046, doi:10.1029/91JD02728, 1992.

Borrmann, S., Kunkel, D., Weigel, R., Minikin, A., Deshler, T., Wilson, J. C., Curtius, J., Volk, C. M., Homan, C. D., Ulanovsky, A., Ravegnani, F., Viciani, S., Shur, G. N., Belyaev, G. V., Law, K. S., and Cairo, F.: Aerosols in the tropical and subtropical UT/LS: in-situ measurements of submicron particle abundance and volatility, Atmos. Chem. Phys., 10, 5573–5592, doi:10.5194/acp-10-5573-2010, 2010.

Brunner, D., Siegmund, P., May, P. T., Chappel, L., Schiller, C., Müller, R., Peter, T., Fueglistaler, S., MacKenzie, A. R., Fix, A., Schlager, H., Allen, G., Fjæraa, A. M., Streibel, M., and Harris, N. R. P.: The SCOUT-O3 Darwin Aircraft Campaign: rationale and meteorology, Atmos. Chem. Phys., 9, 93–117, doi:10.5194/acp-9-93-2009, 2009.

Buontempo, C., Cairo, F., Di Donfrancesco, G., Morbidini, R., Viterbini, M., and Adriani, A.: Optical measurements of atmospheric particles from airborne platforms: in situ and remote sensing instruments for balloons and aircrafts, Ann. Geophys., 49, 57–64, doi:10.4401/ag-3149, 2006.

Cairo, F., Adriani, A., Viterbini, M., Di Donfrancesco, G., Mitev, V., Matthey, R., Bastiano, M., Redaelli, G., Dragani, R., Ferretti, R., Rizi, V., Paolucci, T., Bernardini, L., Cacciani, M., Pace, G., and Fiocco, G.: Polar stratospheric clouds observed during the Airborne Polar Experiment – Geophysica Aircraft in Antarctica (APE-GAIA) campaign, J. Geophys. Res., 109, D07204, doi:10.1029/2003JD003930, 2004.

Cairo, F., Di Donfrancesco, G., Snels, M., Fierli, F., Viterbini, M., Borrmann, S., and Frey, W.: A comparison of light backscattering and particle size distribution measurements in tropical cirrus clouds, Atmos. Meas. Tech., 4, 557–570, doi:10.5194/amt-4-557-2011, 2011.

Carbone, R. E., Wilson, J. W., Keenan, T. D., and Hacker, J. M.: Tropical island convection in the absence of significant topography. Part I: Life cycle of diurnally forced convection, Mon. Weather Rev., 128, 3459–3480, doi:10.1175/1520-0493(2000)128<3459:TICITA>2.0.CO;2, 2000.

Chemel, C., Russo, M. R., Pyle, J. A., Sokhi, R. S., and Schiller, C.: Quantifying the Imprint of a Severe Hector Thunderstorm during ACTIVE/SCOUT-O3 onto the Water Content in the Up-

per Troposphere/Lower Stratosphere, Mon. Weather Rev., 137, 2493–2514, doi:10.1175/2008MWR2666.1, 2009.

Connolly, P. J., Vaughan, G., May, P. T., Chemel, C., Allen, G., Choularton, T. W., Gallagher, M. W., Bower, K. N., Crosier, J., and Dearden, C.: Can aerosols influence deep tropical convection? Aerosol indirect effects in the Hector island thunderstorm, Q. J. Roy. Meteor. Soc., 139, 2190–2208, doi:10.1002/qj.2083, 2013.

Corti, T., Luo, B. P., Fu, Q., Vömel, H., and Peter, T.: The impact of cirrus clouds on tropical troposphere-to-stratosphere transport, Atmos. Chem. Phys., 6, 2539–2547, doi:10.5194/acp-6-2539-2006, 2006.

Corti, T., Luo, B. P., de Reus, M., Brunner, D., Cairo, F., Mahoney, M. J., Martucci, G., Matthey, R., Mitev, V., dos Santos, F. H., Schiller, C., Shur, G., Sitnikov, N. M., Spelten, N., Vössing, H. J., Borrmann, S., and Peter, T.: Unprecedented evidence for deep convection hydrating the tropical stratosphere, Geophys. Res. Lett., 35, L10810, doi:10.1029/2008GL033641, 2008.

Curtius, J., Weigel, R., Vössing, H. J., Wernli, H., Werner, A., Volk, C. M., Konopka, P., Krebsbach, M., Schiller, C., Roiger, A., Schlager, H., Dreiling, V., and Borrmann, S.: Observations of meteoric material and implications for aerosol nucleation in the winter Arctic lower stratosphere derived from in situ particle measurements, Atmos. Chem. Phys., 5, 3053–3069, doi:10.5194/acp-5-3053-2005, 2005.

Davis, S., Hlavka, D., Jensen, E., Rosenlof, K., Yang, Q., Schmidt, S., Borrmann, S., Frey, W., Lawson, P., Vömel, H., and Bui, T. P.: In situ and lidar observations of tropopause subvisible cirrus clouds during TC4, J. Geophys. Res., 115, D00J17, doi:10.1029/2009JD013093, 2010.

de Reus, M., Borrmann, S., Bansemer, A., Heymsfield, A. J., Weigel, R., Schiller, C., Mitev, V., Frey, W., Kunkel, D., Kürten, A., Curtius, J., Sitnikov, N. M., Ulanovsky, A., and Ravegnani, F.: Evidence for ice particles in the tropical stratosphere from in-situ measurements, Atmos. Chem. Phys., 9, 6775–6792, doi:10.5194/acp-9-6775-2009, 2009.

Field, P. R., Heymsfield, A. J., and Bansemer, A.: Shattering and Particle Interarrival Times Measured by Optical Array Probes in Ice Clouds, J. Atmos. Ocean. Tech., 23, 1357–1371, doi:10.1175/JTECH1922.1, 2006.

Frey, W., Borrmann, S., Kunkel, D., Weigel, R., de Reus, M., Schlager, H., Roiger, A., Voigt, C., Hoor, P., Curtius, J., Krämer, M., Schiller, C., Volk, C. M., Homan, C. D., Fierli, F., Di Donfrancesco, G., Ulanovsky, A., Ravegnani, F., Sitnikov, N. M., Viciani, S., D'Amato, F., Shur, G. N., Belyaev, G. V., Law, K. S., and Cairo, F.: In situ measurements of tropical cloud properties in the West African Monsoon: upper tropospheric ice clouds, Mesoscale Convective System outflow, and subvisual cirrus, Atmos. Chem. Phys., 11, 5569–5590, doi:10.5194/acp-11-5569-2011, 2011.

Fueglistaler, S., Dessler, A. E., Dunkerton, T. J., Folkins, I., Fu, Q., and Mote, P. W.: Tropical tropopause layer, Rev. Geophys., 47, RG1004, doi:10.1029/2008RG000267, 2009.

Gallagher, M. W., Connolly, P. J., Crawford, I., Heymsfield, A., Bower, K. N., Choularton, T. W., Allen, G., Flynn, M. J., Vaughan, G., and Hacker, J.: Observations and modelling of microphysical variability, aggregation and sedimentation in tropical anvil cirrus outflow regions, Atmos. Chem. Phys., 12, 6609–6628, doi:10.5194/acp-12-6609-2012, 2012.

Garrett, T. J., Gerber, H., Baumgardner, D. G., Twohy, C. H., and Weinstock, E. M.: Small, highly reflective ice crystals in low-latitude cirrus, Geophys. Res. Lett., 30, 2132, doi:10.1029/2003GL018153, 2003.

Golding, B.: An efficient non-hydrostatic forecast model, Meteorol. Atmos. Phys., 50, 89–103, doi:10.1007/BF01025507, 1992.

Heymsfield, A. J.: Properties of tropical and midlatitude ice cloud particle ensembles. Part I: Median mass diameters and terminal velocities, J. Atmos. Sci., 60, 2573–2591, doi:10.1175/1520-0469(2003)060<2573:POTAMI>2.0.CO;2, 2003.

Heymsfield, A. J., Lewis, S., Bansemer, A., Iaquinta, J., Miloshevich, L. M., Kajikawa, M., Twohy, C., and Poellot, M. R.: A General Approach for Deriving the Properties of Cirrus and Stratiform Ice Cloud Particles, J. Atmos. Sci., 59, 3–29, doi:10.1175/1520-0469(2002)059<0003:AGAFDT>2.0.CO;2, 2002.

Heymsfield, A. J., Miloshevich, L. M., Schmitt, C., Bansemer, A., Twohy, C., Poellot, M. R., Fridlind, A., and Gerber, H.: Homogeneous ice nucleation in subtropical and tropical convection and its influence on cirrus anvil microphysics, J. Atmos. Sci., 62, 41–64, doi:10.1175/JAS-3360.1, 2005.

Heymsfield, A. J., Bansemer, A., Heymsfield, G., and Fierro, A. O.: Microphysics of Maritime Tropical Convective Updrafts at Temperatures from −20 degrees to −60 degrees C, J. Atmos. Sci., 66, 3530–3562, doi:10.1175/2009JAS3107.1, 2009.

Jensen, E. J., Toon, O. B., Selkirk, H. B., Spinhirne, J. D., and Schoeberl, M. R.: On the formation and persistence of subvisible cirrus clouds near the tropical tropopause, J. Geophys. Res., 101, 21361–21375, doi:10.1029/95JD03575, 1996.

Jensen, E. J., Pfister, L., Bui, T. V., Lawson, P., Baker, B., Mo, Q., Baumgardner, D., Weinstock, E. M., Smith, J. B., Moyer, E. J., Hanisco, T. F., Sayres, D. S., Clair, J. M. S., Alexander, M. J., Toon, O. B., and Smith, J. A.: Formation of large (similar or equal to 100 μm) ice crystals near the tropical tropopause, Atmos. Chem. Phys., 8, 1621–1633, doi:10.5194/acp-8-1621-2008, 2008.

Jensen, E. J., Diskin, G., Lawson, R. P., Lance, S., Bui, T. P., Hlavka, D., McGill, M., Pfister, L., Toon, O. B., and Gao, R.: Ice nucleation and dehydration in the Tropical Tropopause Layer, PNAS, 110, 2041–2046, doi:10.1073/pnas.1217104110, 2013.

Keenan, T. D., Ferrier, B., and Simpson, J.: Development and Structure of A Maritime Continent Thunderstorm, Meteorol. Atmos. Phys., 53, 185–222, doi:10.1007/BF01029612, 1994.

Khaykin, S., Pommereau, J.-P., Korshunov, L., Yushkov, V., Nielsen, J., Larsen, N., Christensen, T., Garnier, A., Lukyanov, A., and Williams, E.: Hydration of the lower stratosphere by ice crystal geysers over land convective systems, Atmos. Chem. Phys., 9, 2275–2287, doi:10.5194/acp-9-2275-2009, 2009.

Koop, T., Luo, B., Tsias, A., and Peter, T.: Water activity as the determinant for homogeneous ice nucleation in aqueous solutions, Nature, 406, 611–614, doi:10.1038/35020537, 2000.

Koren, I., Remer, L. A., Kaufman, Y. J., Rudich, Y., and Martins, J. V.: On the twilight zone between clouds and aerosols, Geophys. Res. Lett., 34, L08805, doi:10.1029/2007GL029253, 2007.

Krämer, M., Schiller, C., Afchine, A., Bauer, R., Gensch, I., Mangold, A., Schlicht, S., Spelten, N., Sitnikov, N., Borrmann, S., de Reus, M., and Spichtinger, P.: Ice supersaturations and cirrus cloud crystal numbers, Atmos. Chem. Phys., 9, 3505–3522, doi:10.5194/acp-9-3505-2009, 2009.

Krüger, K., Tegtmeier, S., and Rex, M.: Variability of residence time in the Tropical Tropopause Layer during Northern Hemisphere winter, Atmos. Chem. Phys., 9, 6717–6725, doi:10.5194/acp-9-6717-2009, 2009.

Law, K. S., Fierli, F., Cairo, F., Schlager, H., Borrmann, S., Streibel, M., Real, E., Kunkel, D., Schiller, C., Ravegnani, F., Ulanovsky, A., D'Amato, F., Viciani, S., and Volk, C. M.: Air mass origins influencing TTL chemical composition over West Africa during 2006 summer monsoon, Atmos. Chem. Phys., 10, 10753–10770, doi:10.5194/acp-10-10753-2010, 2010.

Liu, L. and Mishchenko, M. I.: Constraints on PSC particle microphysics derived from lidar observations, J. Quant. Spectrosc. Ra., 70, 817–831, doi:10.1016/S0022-4073(01)00048-6, 2001.

Massie, S., Gettelman, A., Randel, W., and Baumgardner, D.: Distribution of tropical cirrus in relation to convection, J. Geophys. Res.-Atmos., 107, 4591, doi:10.1029/2001JD001293, 2002.

McFarquhar, G. M. and Heymsfield, A. J.: Parameterization of Tropical Cirrus Ice Crystal Size Distributions and Implications for Radiative Transfer: Results from CEPEX, J. Atmos. Sci., 54, 2187–2200, doi:10.1175/1520-0469(1997)054<2187:POTCIC>2.0.CO;2, 1997.

McFarquhar, G. M., Heymsfield, A. J., Spinhirne, J., and Hart, B.: Thin and subvisual tropopause tropical cirrus: Observations and radiative impacts, J. Atmos. Sci., 57, 1841–1853, doi:10.1175/1520-0469(2000)057<1841:TASTTC>2.0.CO;2, 2000.

Measures, R.: Laser Remote Sensing: Fundamentals and Applications, Wiley-Interscience publication, John Wiley & Sons, University of Minnesota, 510 pp., 1984.

Mekonnen, A., Thorncroft, C. D., and Aiyyer, A. R.: Analysis of convection and its association with African easterly waves, J. Climate, 19, 5405–5421, doi:10.1175/JCLI3920.1, 2006.

Mitev, V., Matthey, R., and Makanov, V.: Miniature backscatter lidar for cloud and aerosol observation from high altitude aircraft, Rec. Res. Dev. Geophys, 4, 207–223, doi:10.1127/0941-2948/2005/0046, 2002.

Noel, V., Winker, D. M., McGill, M., and Lawson, P.: Classification of particle shapes from lidar depolarization ratio in convective ice clouds compared to in situ observations during CRYSTAL-FACE, J. Geophys. Res., 109, D24213, doi:10.1029/2004JD004883, 2004.

Park, S., Jimenez, R., Daube, B. C., Pfister, L., Conway, T. J., Gottlieb, E. W., Chow, V. Y., Curran, D. J., Matross, D. M., Bright, A., Atlas, E. L., Bui, T. P., Gao, R. S., Twohy, C. H., and Wofsy, S. C.: The CO2 tracer clock for the Tropical Tropopause Layer, Atmos. Chem. Phys., 7, 3989–4000, doi:10.5194/acp-7-3989-2007, 2007.

Rosenfield, J. E., Considine, D. B., Schoeberl, M. R., and Browell, E. V.: The impact of subvisible cirrus clouds near the tropical tropopause on stratospheric water vapor, Geophys. Res. Lett., 25, 1883–1886, doi:10.1029/98GL01294, 1998.

Saito, K., Keenan, T., Holland, G., and Puri, K.: Numerical simulation of the diurnal evolution of tropical island convection over the Maritime Continent, Mon. Weather Rev., 129, 378–400, doi:10.1175/1520-0493(2001)129<0378:NSOTDE>2.0.CO;2, 2001.

Shur, G., Sitnikov, N., and Drynkov, A.: A mesoscale structure of meteorological fields in the tropopause layer and in the lower stratosphere over the southern tropics (Brazil), Russ. Meteorol. Hydrol., 32, 487–494, doi:10.3103/S106837390708002X, 2007.

Sitnikov, N. M., Yushkov, V. A., Afchine, A. A., Korshunov, L. I., Astakhov, V. I., Ulanovskii, A. E., Krämer, M., Mangold, A., Schiller, C., and Ravegnani, F.: The FLASH instrument for water vapor measurements on board the high-altitude airplane, Instrum. Exp. Tech., 50, 113–121, doi:10.1134/S0020441207010174, 2007.

Skamarock, W. C., Klemp, J. B., Dudhia, J., Gill, D. O., Barker, M., Duda, K. G., Huang, X. Y., Wang, W., and Powers, J. G.: A description of the Advanced Research WRF Version 3, Tech. rep., National Center for Atmospheric Research, 2008.

Sokolov, L. and Lepuchov, B.: Protocol of interaction between Unit for Connection with Scientific Equipment (UCSE) and on-board scientific equipment of Geophysica aircraft (Second edition), Myasishchev Design Bureau (MDB), 1998.

Solomon, S., Borrmann, S., Garcia, R. R., Portmann, R., Thomason, L., Poole, L. R., Winker, D., and McCormick, M. P.: Heterogeneous chlorine chemistry in the tropopause region, J. Geophys. Res.-Atmos., 102, 21411–21429, doi:10.1029/97JD01525, 1997.

Solomon, S., Thompson, D. W. J., Portmann, R. W., Oltmans, S. J., and Thompson, A. M.: On the distribution and variability of ozone in the tropical upper troposphere: Implications for tropical deep convection and chemical-dynamical coupling, Geophys. Res. Lett., 32, L23813, doi:10.1029/2005GL024323, 2005.

Spichtinger, P. and Krämer, M.: Tropical tropopause ice clouds: a dynamic approach to the mystery of low crystal numbers, Atmos. Chem. Phys., 13, 9801–9818, doi:10.5194/acp-13-9801-2013, 2013.

Stith, J. L., Haggerty, J. A., Heymsfield, A., and Grainger, C. A.: Microphysical Characteristics of Tropical Updrafts in Clean Conditions, J. Appl. Meteorol., 43, 779–794, doi:10.1175/2104.1, 2004.

Thomas, A., Borrmann, S., Kiemle, C., Cairo, F., Volk, M., Beuermann, J., Lepuchov, B., Santacesaria, V., Matthey, R., Rudakov, V., Yushkov, V., MacKenzie, A. R., and Stefanutti, L.: In situ measurements of background aerosol and subvisible cirrus in the tropical tropopause region, J. Geophys. Res., 107, 4763, doi:10.1029/2001JD001385, 2002.

Thompson, A., Tao, W., Pickering, K., Scala, J., and Simpson, J.: Tropical deep convection and ozone formation, B. Am. Meteorol. Soc., 78, 1043–1054, doi:10.1175/1520-0477(1997)078<1043:TDCAOF>2.0.CO;2, 1997.

Ulanovsky, A. E., Yushkov, V. A., Sitnikov, N. M., and Ravegnani, F.: The FOZAN-II fast-response chemiluminescent airborne ozone analyzer, Instrum. Exp. Tech., 44, 249–256, doi:10.1023/A:1017535608026, 2001.

van Diedenhoven, B., Fridlind, A. M., Ackerman, A. S., and Cairns, B.: Evaluation of Hydrometeor Phase and Ice Properties in Cloud-Resolving Model Simulations of Tropical Deep Convection Using Radiance and Polarization Measurements, J. Atmos. Sci., 69, 3290–3314, doi:10.1175/JAS-D-11-0314.1, 2012.

Vardiman, L.: The Generation of Secondary Ice Particles in Clouds by Crystal-Crystal Collision, J. Atmos. Sci., 35, 2168–2180, doi:10.1175/1520-0469(1978)035<2168:TGOSIP>2.0.CO;2, 1978.

von Hobe, M., Grooß, J.-U., Günther, G., Konopka, P., Gensch, I., Krämer, M., Spelten, N., Afchine, A., Schiller, C., Ulanovsky, A., Sitnikov, N., Shur, G., Yushkov, V., Ravegnani, F., Cairo, F.,

Roiger, A., Voigt, C., Schlager, H., Weigel, R., Frey, W., Borrmann, S., Müller, R., and Stroh, F.: Evidence for heterogeneous chlorine activation in the tropical UTLS, Atmos. Chem. Phys., 11, 241–256, doi:10.5194/acp-11-241-2011, 2011.

Weigel, R., Hermann, M., Curtius, J., Voigt, C., Walter, S., Böttger, T., Lepukhov, B., Belyaev, G., and Borrmann, S.: Experimental characterization of the COndensation PArticle counting System for high altitude aircraft-borne application, Atmos. Meas. Tech., 2, 243–258, doi:10.5194/amt-2-243-2009, 2009.

Weigel, R., Borrmann, S., Kazil, J., Minikin, A., Stohl, A., Wilson, J. C., Reeves, J. M., Kunkel, D., de Reus, M., Frey, W., Lovejoy, E. R., Volk, C. M., Viciani, S., D'Amato, F., Schiller, C., Peter, T., Schlager, H., Cairo, F., Law, K. S., Shur, G. N., Belyaev, G. V., and Curtius, J.: In situ observations of new particle formation in the tropical upper troposphere: the role of clouds and the nucleation mechanism, Atmos. Chem. Phys., 11, 9983–10010, doi:10.5194/acp-11-9983-2011, 2011.

Wen, G., Marshak, A., and Cahalan, R.: Impact of 3-D clouds on clear-sky reflectance and aerosol retrieval in a biomass burning region of Brazil, IEEE Geosci. Remote S., 3, 169–172, doi:10.1109/LGRS.2005.861386, 2006.

Winker, D. M. and Trepte, C. R.: Laminar cirrus observed near the tropical tropopause by LITE, Geophys. Res. Lett., 25, 3351–3354, doi:10.1029/98GL01292, 1998.

Yano, J.-I. and Phillips, V. T. J.: Ice-Ice Collisions: An Ice Multiplication Process in Atmospheric Clouds, J. Atmos. Sci., 68, 322–333, doi:10.1175/2010JAS3607.1, 2011.

Yushkov, V., Oulanovsky, A., Lechenuk, N., Roudakov, I., Arshinov, K., Tikhonov, F., Stefanutti, L., Ravegnani, F., Bonafe, U., and Georgiadis, T.: A Chemiluminescent Analyzer for Stratospheric Measurements of the Ozone Concentration (FOZAN), J. Atmos. Ocean. Tech., 16, 1345–1350, doi:10.1175/1520-0426(1999)016<1345:ACAFSM>2.0.CO;2, 1999.